HAL
open science

Charge transport and magnetization profile at the interface between the correlated metal CaRuO3 and the antiferromagnetic insulator CaMnO3

J. W. Freeland, J. Chakhalian, A. V. Boris, Jean-Marc Tonnerre, J.J. Kavich, P. Yordanov, Stéphane Grenier, P. Zschack, E. Karapetrova, P. Popovich, et al.

To cite this version:

J. W. Freeland, J. Chakhalian, A. V. Boris, Jean-Marc Tonnerre, J.J. Kavich, et al.. Charge transport and magnetization profile at the interface between the correlated metal CaRuO3 and the antiferromagnetic insulator CaMnO3. Physical Review B: Condensed Matter and Materials Physics (1998-2015), 2010, 81 (9), pp.094414. 10.1103/PhysRevB.81.094414 . hal-00982590

HAL Id: hal-00982590

https://hal.science/hal-00982590v1

Submitted on 16 Mar 2022

HAL is a multi-disciplinary open access archive for the deposit and dissemination of scientific research documents, whether they are published or not. The documents may come from teaching and research institutions in France or abroad, or from public or private research centers.

L'archive ouverte pluridisciplinaire **HAL**, est destinée au dépôt et à la diffusion de documents scientifiques de niveau recherche, publiés ou non, émanant des établissements d'enseignement et de recherche français ou étrangers, des laboratoires publics ou privés.

PHYSICAL REVIEW B **81**, 094414 (2010)

Charge transport and magnetization profile at the interface between the correlated metal $CaRuO_3$ and the antiferromagnetic insulator $CaMnO_3$

J. W. Freeland,[1] J. Chakhalian,[2] A. V. Boris,[3,4] J.-M. Tonnerre,[5] J. J. Kavich,[1,6] P. Yordanov,[3] S. Grenier,[5] P. Zschack,[1] E. Karapetrova,[1] P. Popovich,[3] H. N. Lee,[7] and B. Keimer[3]

[1]*Advanced Photon Source, Argonne National Laboratory, Argonne, Illinois 60439, USA*
[2]*Department of Physics, University of Arkansas, Fayetteville, Arkansas 72701, USA*
[3]*Max-Planck-Institut für Festkörperforschung, D-70569 Stuttgart, Germany*
[4]*Department of Physics, Loughborough University, Loughborough LE11 3TU, United Kingdom*
[5]*Institut Néel, CNRS and Université Joseph Fourier, Boite Postale 166, F-38043 Grenoble Cedex 9, France*
[6]*Department of Physics, University of Illinois at Chicago, Chicago, Illinois 60607, USA*
[7]*Materials Science and Technology Division, Oak Ridge National Laboratory, Oak Ridge, Tennessee 37831, USA*

(Received 1 June 2009; revised manuscript received 29 January 2010; published 12 March 2010)

A combination of spectroscopic probes was used to develop a detailed experimental description of the transport and magnetic properties of superlattices composed of the paramagnetic metal $CaRuO_3$ and the antiferromagnetic insulator $CaMnO_3$. The charge-carrier density and Ru valence state in the superlattices are not significantly different from those of bulk $CaRuO_3$. The small charge transfer across the interface implied by these observations confirms predictions derived from density-functional calculations. However, a ferromagnetic polarization due to canted Mn spins penetrates 3–4 unit cells into $CaMnO_3$, far exceeding the corresponding predictions. The discrepancy may indicate the formation of magnetic polarons at the interface.

DOI: 10.1103/PhysRevB.81.094414 PACS number(s): 75.70.Cn, 73.20.−r, 73.21.Cd

Recent advances in the atomic-scale control of transition-metal oxide interfaces offer new opportunities for the manipulation of strongly correlated electron systems. While first device applications are being explored,[1] there is growing awareness of the wealth of microscopic phenomena that need to be understood in order to arrive at a quantitative description of the electronic state at oxide interfaces. These include the polarity of the atomic layers comprising the interface,[2] lattice relaxations (which are particularly important for ferroelectric and quantum paraelectric materials),[3] orbital reconstructions induced by misfit strain[4] and/or covalent bonding across the interface,[5] magnetic polarization due to the reduced coordination of magnetic atoms and/or exchange interactions across the interface,[6] and interface-specific disorder. This calls for simple model systems in which individual issues can be isolated, and the results of theoretical and experimental studies of buried interfaces can be quantitatively compared. A model system that has received particular recent attention is the weakly correlated metallic state at the interface between the band insulators $SrTiO_3$ and $LaAlO_3$, whose properties are controlled by interface polarity and lattice relaxations although there is still an ongoing debate about the role of defects (see Ref. 7, and references therein).

Another problem of fundamental interest is the interface between a correlated metallic state and an antiferromagnetic insulator, two of the most extensively investigated ground states of bulk transition-metal oxides. As theoretical research is beginning to address the length scales for the intermixing of metallicity and antiferromagnetic order in this situation,[8,9] the interface between the correlated paramagnetic metal $CaRuO_3$ (CRO) (Refs. 10–12) and the antiferromagnetic insulator $CaMnO_3$ (CMO) (Ref. 13) is emerging as a model system where these issues can be explored experimentally without interference from interface polarity, incipient ferroelectricity, extensive disorder or misfit strain, and orbital degeneracy. Whereas bulk $CaMnO_3$ is a *G*-type antiferromagnet (that is, the Mn spin orientation alternates along all nearest-neighbor bond directions of the nearly cubic perovskite lattice), prior magnetometry,[14] and magneto-optical[15] studies of $CaRuO_3$-$CaMnO_3$ superlattices revealed a ferromagnetic moment centered at the interface. Based on density-functional calculations, this was attributed to leakage of a small number of itinerant electrons from $CaRuO_3$ into the first atomic layer of $CaMnO_3$, where they actuate a ferromagnetic double-exchange interaction and induce canting of the Mn spins.[9]

In this paper, we combine several spectroscopic and scattering probes of $CaRuO_3$-$CaMnO_3$ superlattices including far-infrared (FIR) spectral ellipsometry, x-ray absorption spectroscopy (XAS), x-ray magnetic circular dichroism (XMCD), and x-ray resonant magnetic scattering (XRMS) in order to develop a comprehensive experimental description of the charge transport properties, as well as the valence state and magnetic polarization of Ru and Mn atoms near the interface. We find that the charge transfer across the interface is small, and that the net magnetization of the superlattices arises mostly from canted Mn spins near the interface, confirming corresponding predictions of the density-functional calculations.[9] Surprisingly, however, the penetration depth of the ferromagnetic polarization in $CaMnO_3$ is 3–4 unit cells (u.c.'s), greatly exceeding the theoretically predicted length scale of 1 u.c. Based on an analogy to lightly doped bulk $CaMnO_3$, we attribute the large ferromagnetic penetration depth to polaronic effects not included in the calculations.

I. EXPERIMENT

A series of superlattices (SL), $LaAlO_3(001)/[CaMnO_3(10\ \text{uc})/CaRuO_3(N\ \text{uc})]_6$ with

 ©2010 The American Physical Society

$N=4$ to 10 consecutive $CaRuO_3$ unit cells, were grown by pulsed laser deposition with a KrF excimer laser ($\lambda=248$ nm, $J=1$ J/cm^2) at a substrate temperature of 720 °C in 10 mTorr of pure oxygen, using stoichiometric sintered targets. Upon deposition, all samples were *in situ* annealed in 50–100 mTorr of oxygen for 5–10 min and then gradually cooled down to room temperature. Reflection high-energy electron-diffraction (RHEED) oscillations observed *in situ*, as well as spectroscopic data and XRMS profiles taken on the finished specimens, demonstrate flat, atomically sharp interfaces. X-ray diffraction measurements were made at beamline 33-BM of the Advanced Photon Source with a photon energy of 8.4 keV. The FIR experiments were conducted at beamline IR1 at the ANKA synchrotron in Karlsruhe, Germany,[16] with angles of incidence ranging from 70° to 85°. The XAS and XMCD measurements were performed at beamline 4-ID-C of the Advanced Photon Source, with magnetic fields of up to 7 T applied in the plane of the superlattices. The measurements were performed by monitoring the intensity, I, of left (−) and right (+) circularly polarized x rays absorbed by the specimen using the surface/interface sensitive total-electron-yield detection described previously.[5,6] The sum, $I^+ + I^-$, yields the XAS signal while the XMCD signal is derived from the difference, $I^+ - I^-$. The XRMS experiments were carried out at the SIM beamline at the Swiss Light Source using the RESOXS chamber.[17] The reflected intensities I^+ and I^- were collected for two opposite directions of a magnetic field applied along the intersection of the superlattice and scattering planes. The amplitude of the magnetic field available in the chamber is 0.16 T, which sufficient to field cool the sample into a partially magnetized state with a net magnetization of ~25% of the saturation value.

II. STRUCTURE AND TRANSPORT

RHEED patterns during growth show the growth occurs via atomically smooth layer-by-layer deposition [see Fig. 1(a)]. X-ray diffraction measurements shown in Fig. 1(b) provide a picture of the superlattice structure for the $N=10$ uc sample. The film has a well-defined Bragg peak corresponding to $c_{film}=3.826$ Å, which in a superlattice is the average of the two constituents. Since the films are completely lattice matched to $LaAlO_3$ (LAO) [see Fig. 1(c)], the c-axis parameter under strain for the individual layers can be estimated assuming a Poisson ratio =1/3, which seems to be valid for many oxide films.[18–20] The average lattice parameter is consistent with a ratio of thicknesses for CMO and CRO that is close to one as expected for the CMO(10 u.c.)/CRO(10 u.c.) sample. The film shows clear superlattice peaks near the (001) Bragg peak with a spacing corresponding to a ~76 Å bilayer thickness, which is in good agreement with the soft x-ray reflectivity data discussed below. The Kiessig fringes demonstrate a high-quality superlattice, and indicate a total film thickness of ~460 Å, as expected from six repeats of a 76-Å-thick bilayer. The asymmetry in the superlattice peak intensities results from the strain gradient within the structure since CMO is under tensile strain while CRO is under compressive strain.[21]

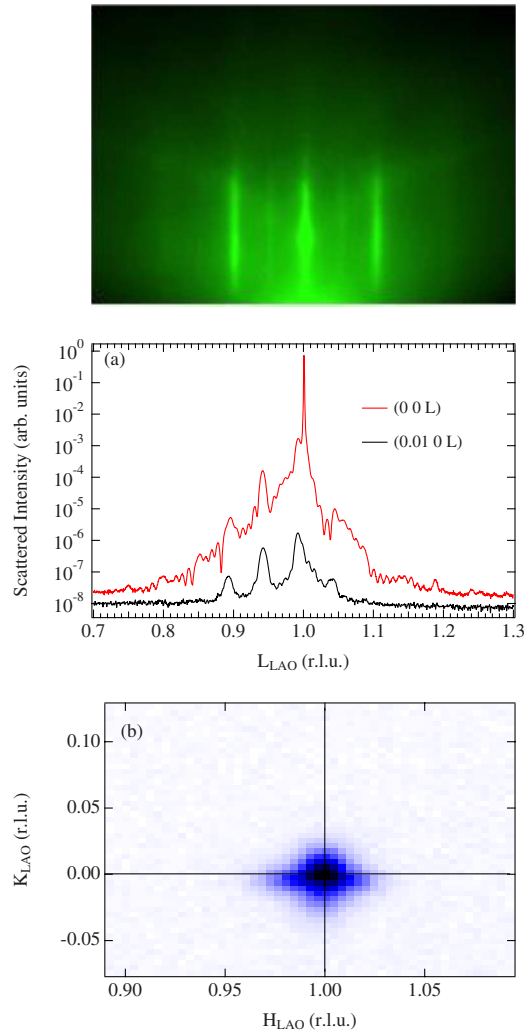

FIG. 1. (Color online) (a) Reflection high-energy electron-diffraction pattern after growth of the final layer for the $N=10$ u.c. sample. (b) (H0L) scan for the $N=10$ u.c. sample on ($H=0$) and slightly off ($H=0.01$) the specular rod. (c) HK map on the film (003) Bragg peak showing that the $N=10$ u.c. sample is fully lattice matched to the LAO substrate.

As shown in Fig. 2, in the dc limit, the superlattices show evidence of localization of the carriers at low temperature even when the CRO layer is as thick as 10 u.c. (~4 nm).

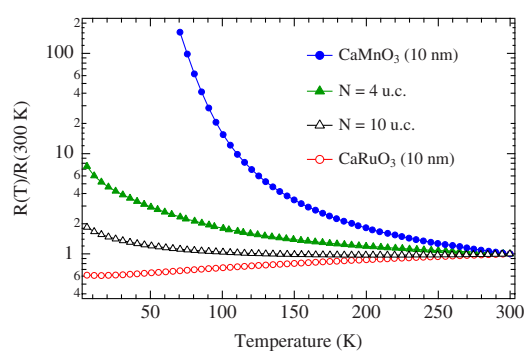

FIG. 2. (Color online) Normalized sheet resistance of CMO-CRO superlattices as a function of temperature.

This weakly insulating behavior is in marked contrast with the bulk CRO behavior where the metallic state is observed even for the 10 nm single-layer film. The trend, however, indicates that the SLs are tending toward a transition to metallic behavior with increasing CRO layer thicknesses. While the lowest temperatures shows activated hopping transport, in the range of $T \sim 10-100$ K both samples show a $\Delta R/R = A \ln(1/T)$ behavior. This behavior has been seen in ultrathin films[22] and underdoped cuprates,[23,24] and attributed to Anderson localization of the carriers. One important point to note is that for Anderson localization, there may still be states at the Fermi level but they are localized. From the optical measurements discussed below, it will be seen that the behavior is consistent with inhomogeneous conduction perhaps via weakly connected metallic regions in the CRO layer.

III. OPTICAL CONDUCTIVITY

The charge transport properties of the $CaRuO_3$-$CaMnO_3$ superlattices were determined by FIR ellipsometry, which yields the frequency-dependent complex dielectric function from the ellipsometric angles, $\Psi(\omega)$ and $\Delta(\omega)$, without the need for reference measurements and Kramers-Kronig transformations. In contrast to dc transport experiments, this method is insensitive to the influence of substrate-induced steps or strain-induced dislocations on the current flow through the atomically thin layers, and it avoids complications arising from the attachment of electrical contacts. The ellipsometric angles Ψ and Δ are defined through the complex Fresnel reflection coefficients for light polarized parallel (r_p) and perpendicular (r_s) to the plane of incidence,

$$\tan \Psi e^{i\Delta} = \frac{r_p}{r_s}. \quad (1)$$

Figure 3 shows the experimental spectra of the $N=10$ superlattice and the near normal-incidence reflectivity spectrum of the bare $LaAlO_3$ substrate. The large contribution of the substrate to the reflectance of SLs prevents direct inversion of the ellipsometric parameters into the superlattice complex conductivity, and numerical regression procedures are needed for data analysis. The complex refractive indices for the substrate were obtained with high accuracy form independent spectroscopic ellipsometry measurements at different temperatures and used in the multilayer characterization procedure. Our reflectivity and ellipsometric data were analyzed with a computer program for the characterization of thin films based on advanced optimization methods providing rapid convergence of the regression procedure[25] by holding the layer thicknesses constant (460 Å as determined from the x-ray reflectivity).

Since the thickness of the superlattices is more than two orders of magnitude smaller than the far-IR wavelength, the entire sample was treated as one single layer according to an effective-medium approximation with a mixture of the ruthenate and manganite layers. Accordingly the pair of complex dielectric functions $\varepsilon_\perp$ and $\varepsilon_\parallel$ of the effective ordinary (in-plane) and extraordinary (c-axis) response of the uniaxial film corresponds to the volume average of the dielectric tensor projections of the bare superlattice components. Because our uniaxial superlattice layer is oriented with the c axis normal to the surface, the component of the dielectric tensor $\varepsilon_\perp$ along the c axis contributes relatively little to the ellipsometrically measured complex reflection coefficients. It allows the inversion of the ellipsometry data to be done within the framework of the easily solved isotropic problem with the complex pseudodielectric function, $\varepsilon^* \simeq \varepsilon_\parallel$. While this procedure is not exact, a full anisotropic analysis using a variety of reasonably possible c-axis dielectric functions showed that the relative difference between ε^* and $\varepsilon_\parallel$ values is less than 10% over the measured spectral range. This estimation is also confirmed by our measurements at multiple angles of incidence. We use below $\varepsilon_1(\omega)+i\varepsilon_2(\omega)$ to denote the effective complex pseudodielectric function of the superlattice when discussing the in-plane dielectric response.

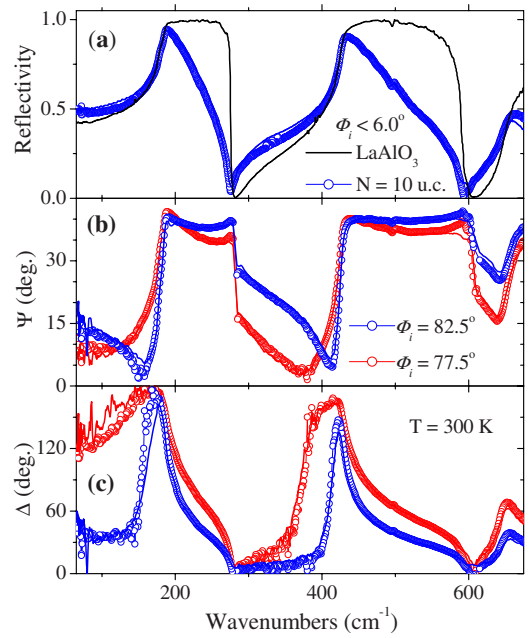

FIG. 3. (Color online) Experimental (solid lines) and best-fit calculated (open circles) (a) near normal-incidence reflectivity and [(b) and (c)] ellipsometry spectra of the $N=10$ superlattice, $T=300$ K. The reflectivity spectra of the bare $LaAlO_3$ substrate is shown for comparison (black solid line). Solid lines in ellipsometry spectra are fits to the model discussed in the text.

The wavelength-by-wavelength regression procedure has been employed to extract the real parts of the dielectric function, ε_1, and the optical conductivity, $\sigma_1=(1/4\pi)\omega\varepsilon_2$. The best-fit calculated spectra of $R(\omega)$, $\Psi(\omega)$, and $\Delta(\omega)$ are shown in Fig. 3 by open circles. Figure 4 shows the resulting $\varepsilon_1(\omega)$ and $\sigma_1(\omega)$ spectra of the $N=4$ and 10 superlattices. Both data sets are well described by a broad Drude response,

$$\varepsilon_1(\omega) + i\varepsilon_2(\omega) = \varepsilon_\infty - \frac{\omega_{pl}^2}{\omega^2 + i\omega\gamma} \quad (2)$$

with a ratio of scattering rate and plasma frequency $\gamma/\omega_{pl} \approx 0.2-0.3$, which is typical for bulk single-crystalline $CaRuO_3$ (dashed lines in Fig. 4). Note that the parameters in the Drude fit are well constrained because both σ_1 and

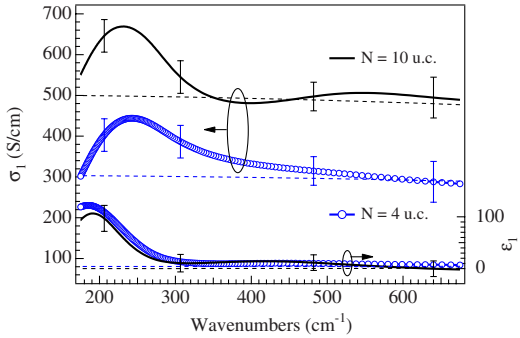

FIG. 4. (Color online) Best-fit model functions $\sigma_1(\omega)$ and $\varepsilon_1(\omega)$ for superlattices with $N=4$ and 10 consecutive $CaRuO_3$ u.c., as obtained from FIR ellipsometry data by inversion of the ellipsometric parameters. The dashed lines represent the results of Drude fits, as described in the text. The peak at 220 cm^{-1} superposed on the broad Drude response is due to a bond-bending lattice vibration of $CaMnO_3$.

ε_1 are available. The effective number of charge carriers per Ru atom extracted from a sum-rule analysis, $N_{\text{eff}}=\frac{2m}{\pi e^2 n_{\text{Ru}}}\frac{\omega_{pl}^2}{8}=0.11\pm0.03$ (where m is the free-electron mass and n_{Ru} the density of Ru atoms), is identical for both $N=4$ and 10 samples. It also agrees (within the measurement error) with the corresponding quantity $N_{\text{eff}}=0.082$ reported for bulk $CaRuO_3$.[10,12] These results indicate that, even in the $N=4$ sample, the conductivity of the metallic layers is not significantly disrupted by Ru-Mn interdiffusion, testifying to the high quality of the interfaces. The theoretical prediction that only ~5% of the charge-carrier density in the $CaRuO_3$ atomic layer closest to the interface is transferred is consistent with our result that the charge transfer, if any, is small. The reduction in the Drude weight corresponding to the predicted charge transfer of this magnitude is within the error of the FIR data.

IV. POLARIZED X-RAY ABSORPTION

The XAS measurements near the Ru L_3 and Mn L_3 absorption edges yield complementary information on the charge transfer across the interface. From a comparison of the absorption profiles (solid lines in Fig. 5) to reference compounds,[26–30] we conclude that both Mn and Ru are close to the 4+ valence state. Specifically, in the $N=4$ sample (where half of the Ru atoms are at the interface), a substantial change in the Ru valence state due to charge transfer across the interface would result in a noticeable multiplet splitting of the Ru absorption peak due to population of e_g orbitals, similar to that seen in compounds containing Ru^{4+}-Ru^{5+} mixtures.[28–30] From the absence of this splitting in the data of Fig. 5, we infer an interfacial Ru valence close to 4+, consistent with the FIR data and with the predictions of Ref. 9.

In agreement with prior work on this system,[14,15] magnetic-susceptibility measurements on both samples indicate a net magnetization upon cooling below 120 K, coincident with the Néel temperature of bulk antiferromagnetic $CaMnO_3$. In order to understand where the magnetism is

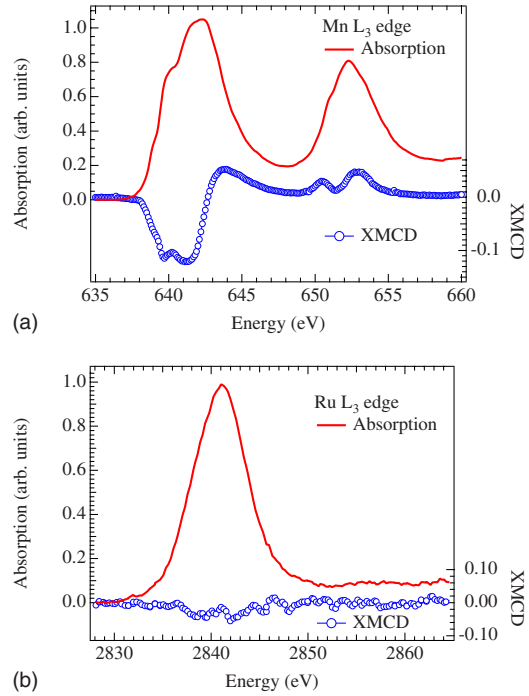

FIG. 5. (Color online) (a) Absorption and XMCD measured at the Mn L_3 edge at $T=10$ K for $N=6$. The XMCD of signal is sizable (~12%) and consistent with rather large magnetic moment. (b) Absorption and XMCD from the Ru L_3 edge for the 4 unit cell $CaRuO_3$ sample. Comparison with reference samples indicates that for both the Mn and Ru, the valence is close to 4+. The very small apparent Ru XMCD signal is within the systematic error of the measurement.(c) Field dependence of the Mn XMCD measured at 10 K showing that the magnetic moment saturates near 4 T but shows no sign of remanent magnetization.

localized in the structure, we turn to XMCD and XRMS measurements. The XMCD signals from the polarized XAS measurements yield information about the contribution of each constituent transition-metal ion to the net magnetization (see Fig. 5). While the Ru XMCD does not exceed 3%, a clear XMCD signal of ~12% is observed at the Mn L edge for both samples in a magnetic field of 7 T and does not seem to depend on N, which is consistent with previous work.[14] Comparison with Ru XMCD references places an upper bound of $\sim0.3\mu_B$ on the net magnetic moment per Ru atom while the Mn XMCD corresponds to a layer-averaged moment of $1\mu_B$ per Mn atom,[31] which implies that the net magnetization is dominated by $CaMnO_3$, consistent with the theoretical work of Ref. 9. The XMCD for both superlattices vanishes upon heating above 100–120 K, the Néel temperature of bulk $CaMnO_3$, yet control measurements on an isolated $CaMnO_3$ film grown on $LaAlO_3$ (not shown) revealed no XMCD signal above background, which implies that the Mn magnetism is due to the CRO/CMO interface and not due to the entire CMO layer.

The Mn XMCD data provides several key points of evidence supporting the theoretically predicted weakened antiferromagnetic state localized near the interface. First, the layer-averaged XMCD signal is substantially lower than expected if the entire CMO layer were fully ferromagnetic

(which would yield $3\mu_B$/Mn atom for Mn^{4+}).[31] Note, however, that based on the XMCD measurements alone we cannot discriminate between a single, fully aligned interface layer and a more extended layer with weaker spin alignment. This will be accomplished by the XRMS measurements described below. The second point is that the XMCD does not exhibit significant hysteresis effects and shows zero remanent moment, consistent with a dominant antiferromagnetic interaction. And the final point is that the interface magnetism disappears at the Néel temperature of $CaMnO_3$, which indicates that it is directly tied to the antiferromagnetic ground state in the bulk of the $CaMnO_3$ layer.

V. X-RAY RESONANT MAGNETIC SCATTERING

In order to determine the length scale of the interface-induced ferromagnetic polarization, we have performed XRMS measurements with circularly polarized x rays at two photon energies in the vicinity of the Mn L_3 absorption edge. The resonant reflectivity in the charge channel $(I^+ + I^-)$ exhibits a series of Bragg peaks characteristic of the superlattice periodicity, separated by interference fringes due the finite thickness of the sample [see Fig. 7(a)]. The first photon energy (620 eV) was chosen to be off-resonance allowing for a structural analysis not reliant on the knowledge of the resonant scattering factor (but rather on the standard, tabulated atomic scattering factor). The second energy (639.2 eV, corresponding to the inflexion point of the absorption edge) was chosen to reduce the x-ray absorption while maximizing the real part of the magnetic scattering factor.[32,33] Analysis of the magnetic structure of the film requires knowledge of the structural parameters of the superlattices (thickness, roughness, and density of the layers), which were derived from a refinement of off-resonant reflectivity data recorded at 620 eV and confirmed by the refinement of the resonant reflectivity using the resonant scattering factor derived from the XAS measurements. Although the fits exhibit some discrepancies with the data between the Bragg peaks, the details of the Bragg peaks are relatively well described.

For the nominally 10 u.c./10 u.c. sample, the layer thicknesses from the structural refinement are 42.1 ± 0.8 Å for the $CaMnO_3$ layer and 33.3 ± 0.6 Å for $CaRuO_3$, which corresponds to a structure of roughly CMO(11 u.c.)/CRO(9 u.c.). The overall roughness is found to be 5 ± 0.5 Å with a slightly larger roughness at the top surface (6–7 Å). Hence, the in-plane averaged value of the roughness corresponds to an order of 1–2 u.c. It is hard to distinguish from reflectivity measurements a situation where at a local scale the interface is actually very sharp (0–1 u.c. step) but localized at different positions along the z axis from a situation where the interface is flat with intermixing over a certain 1–2 u.c. thickness. However, the lack of change in the Ru and Mn electronic structure compared to bulk CRO and CMO strongly disfavors the intermixing alternative and favors sharp interfaces at different heights resulting from the substrate step structure and growth dynamics.

Once the chemical structure was refined, the magnetic profile was probed by the charge-magnetic scattering in the $I^+ - I^-$ signal.[32,33] Figure 7(b) displays the difference $I^+ - I^-$ measured on top of the first four Bragg peaks normalized to the corresponding peak intensity (upper panel) in comparison to the results of simulations for several models of the magnetic profile [see Fig. 7(c)]. For the case of a superlattice, the key point is the q_z evolution due to the cross correlation of the charge and magnetic scattering in the XRMS signal. When the magnetic profile differs from the chemical profile, the sign sequence of the normalized differences varies depending on the thickness of the magnetic layer within the CMO layer [see Fig. 7(c)]. By considering a simple symmetric step profile for the magnetization in $CaMnO_3$, composed of equally thick magnetic layers at the interfaces and a nonmagnetic core layer, we can study the evolution of the sign and gain insight into the thickness of the magnetic layer near the interface.

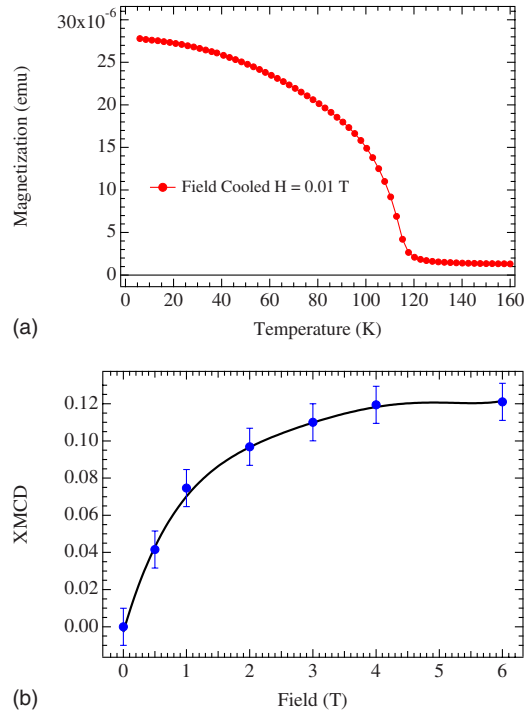

FIG. 6. (Color online) (a) Magnetization versus temperature measured by total moment magnetometry, which show the clear onset of order close to $T_N \sim 120$ K. (b) Field dependence of the Mn XMCD measured at 10 K showing that the magnetic moment saturates near 4 T but shows no sign of remanent magnetization.

The simulated and observed intensities show very good agreement for an interfacial thickness of 1.38 nm (3.5 u.c.). This model reproduces both the experimentally observed sign sequence of $I^+ - I^-$ at the Bragg peaks and its relative amplitude. The absolute magnitude of the normalized difference was calculated with the constraint that its integral equals the XMCD signal discussed above [scaled for the lower applied magnetic field, see Fig. 6(b)]. As shown in Fig. 7(c), the result also agrees closely with the experimental data. Despite its simplicity, the model therefore provides an excellent description of the salient features of the XRMS data. Note that this sign sequence is a strong signature of the extended magnetic profile and cannot be reproduced by a magnetic profile limited to 1 u.c. even considering a distribution of domains with different CRO and CMO thicknesses

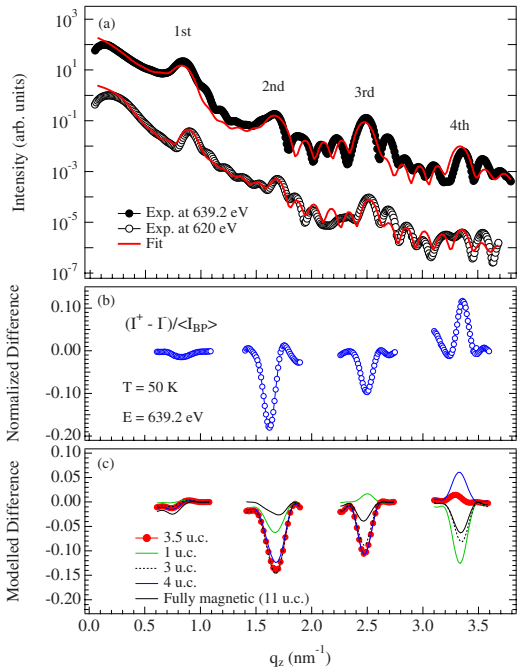

FIG. 7. (Color online) (a) Specular reflectivity measured at 50 K for E=639.2 eV on the Mn L_3 edge (upper trace) and at room temperature with photon energy E=620 eV, below the Mn L_3 edge (lower trace). The lines are the results of fits to a structural model discussed in the text. The Bragg-peak positions are indicated. (b) Dichroic differences $I^+ - I^-$ measured at the Bragg-peak positions, normalized to the peak intensity. (c) Calculated normalized difference at the same Bragg-peak positions for different layer thicknesses of the interface magnetized regions in $CaMnO_3$.

(i.e., 8/11, 10/10, 9/11, 8/12, and 10/11) to account for the effect of an effective roughness. From this we conclude that the ferromagnetic polarization is not limited to the immediate vicinity of the interface, as theoretically predicted[9] but extends further into the CMO layer. Specifically, a model in which the net magnetization arises entirely from the first $CaMnO_3$ unit cell at the interface is ruled out by the behavior of $I^+ - I^-$ at the third- and fourth-order Bragg peaks.

VI. DISCUSSION

Prior work on lightly La-doped bulk $CaMnO_3$ provides clues to the increased length scale of the magnetic interface layer and the origin of the remarkably effective disruption of the antiferromagnetic order by a small density of electrons. Specifically, it was shown that this system exhibits a net magnetization of $\sim 7\mu_B$ for each electron donated by La.[13] Based on transport[34] and neutron-scattering measurements[35] as well as model calculations,[36] this effect was attributed to the formation of a magnetization cloud extending over $\sim$7 Mn sites around the electron due to the ferromagnetic double-exchange interaction it actuates between neighboring Mn spins, in conjunction with local lattice distortions. A closely related "orbital polaron" effect has also been investigated in lightly hole-doped manganates.[37] A similarly extended cloud of polarized Mn spins around electrons transferred across the $CaRuO_3$-$CaMnO_3$ interface would explain the large ferromagnetic penetration depth we observed. Further work is required to assess whether the magnetic polarons form a narrow band, or whether they localize in a charge-ordered state or in the vicinity of defects at the interface. In any case, our results suggest that magnetic polarons, which have been extensively investigated in bulk manganates and other transition-metal oxides, strongly influence the physical properties of oxide interfaces and should therefore be considered in future theoretical work on this issue.

VII. CONCLUSION

In summary, a combination of different spectroscopic probes of $CaRuO_3$-$CaMnO_3$ superlattices with atomically sharp interfaces has enabled a detailed experimental test of theoretical predictions for the interface-induced intermixing of metallicity and magnetic order.[9] Two key predictions were confirmed: first, the density of conduction electrons in the $CaRuO_3$ layers remains equal to that of bulk $CaRuO_3$ even if the layers are only four unit cells thin, which implies only a small leakage of carriers into $CaMnO_3$. Second, the net magnetization arises from canting of Mn moments in $CaMnO_3$, with at most a small contribution from Ru ions in $CaRuO_3$. However, the length scale for the interface-induced ferromagnetic polarization in $CaMnO_3$ exceeds the theoretical prediction by more than a factor of 3, despite the low density of carriers transferred across the interface.

ACKNOWLEDGMENTS

Work at Argonne, including the Advanced Photon Source, and the Center for Nanoscale Materials is supported by the U.S. Department of Energy, Office of Science, under Contract No. DE-AC02-06CH11357. Work in Stuttgart was partially supported by the German Science Foundation under collaborative Grant No. SFB/TRR80. We thank Y.-L. Mathis for the support at ANKA. J.C. was supported by DOD-ARO under Grant No. W911NF-08-1-0186 and NSF under Contract No. DMR-0747808. H.N.L. was sponsored by the Division of Materials Sciences and Engineering, U.S. Department of Energy. Work at SLS is supported by the European Commission under the Sixth Framework Programme: Strengthening the European Research Area, Research Infrastructures, Contract No. RII3-CT-2004-506008.

[1] C. H. Ahn, A. Bhattacharya, M. Di Ventra, J. N. Eckstein, C. D. Frisbie, M. E. Gershenson, A. M. Goldman, I. H. Inoue, J. Mannhart, A. J. Millis, Alberto F. Morpurgo, D. Natelson, and J.-M. Triscone, Rev. Mod. Phys. **78**, 1185 (2006).

[2] N. Nakagawa, H. Y. Hwang, and D. A. Muller, Nature Mater. **5**, 204 (2006).

[3] R. Pentcheva and W. E. Pickett, Phys. Rev. B **78**, 205106 (2008).

[4] A. Tebano, C. Aruta, S. Sanna, P. G. Medaglia, G. Balestrino, A. A. Sidorenko, R. De Renzi, G. Ghiringhelli, L. Braicovich, V. Bisogni, and N. B. Brookes, Phys. Rev. Lett. **100**, 137401 (2008).

[5] J. Chakhalian, J. W. Freeland, H.-U. Habermeier, G. Cristiani, G. Khaliullin, M. van Veenendaal, and B. Keimer, Science **318**, 1114 (2007).

[6] J. Chakhalian, J. W. Freeland, G. Srajer, J. Strempfer, G. Khaliullin, J. C. Cezar, T. Charlton, R. Dalgliesh, C. Bernhard, G. Cristiani, H.-U. Habermeier, and B. Keimer, Nat. Phys. **2**, 244 (2006).

[7] M. Huijben, A. Brinkman, G. Koster, G. Rijnders, H. Hilgenkamp, and D. H. A. Blank, Adv. Mater. (Weinheim, Ger.) **21**, 1665 (2009).

[8] R. W. Helmes, T. A. Costi, and A. Rosch, Phys. Rev. Lett. **101**, 066802 (2008).

[9] B. R. K. Nanda, S. Satpathy, and M. S. Springborg, Phys. Rev. Lett. **98**, 216804 (2007).

[10] S. Kamal, D. M. Kim, C. B. Eom, and J. S. Dodge, Phys. Rev. B **74**, 165115 (2006).

[11] Y. S. Lee, J. Yu, J. S. Lee, T. W. Noh, T.-H. Gimm, H.-Y. Choi, and C. B. Eom, Phys. Rev. B **66**, 041104 (2002).

[12] I. I. Mazin and D. J. Singh, Phys. Rev. B **56**, 2556 (1997); **73**, 189903 (2006).

[13] J. J. Neumeier and J. L. Cohn, Phys. Rev. B **61**, 14319 (2000).

[14] K. S. Takahashi, M. Kawasaki, and Y. Tokura, Appl. Phys. Lett. **79**, 1324 (2001).

[15] H. Yamada, H. Sato, H. Akoh, N. Kida, T. Arima, M. Kawasaki, and Y. Tokura, Appl. Phys. Lett. **92**, 062508 (2008).

[16] C. Bernhard, J. Humlicek, and B. Keimer, Thin Solid Films **455-456**, 143 (2004).

[17] N. Jaouen, J.-M. Tonnerre, G. Kapoujian, P. Taunier, J.-P. Roux, D. Raoux, and F. Sirotti, J. Synchrotron Radiat. **11**, 353 (2004).

[18] R. A. Rao, Q. Gan, C. B. Eom, R. J. Cava, Y. Suzuki, J. J. Krajewski, S. C. Gausepohl, and M. Lee, Appl. Phys. Lett. **70**, 3035 (1997).

[19] D. Fuchs, E. Arac, C. Pinta, S. Schuppler, R. Schneider, and H. v. Lohneysen, Phys. Rev. B **77**, 014434 (2008).

[20] D. L. Proffit, H. W. Jang, S. Lee, C. T. Nelson, X. Q. Pan, M. S. Rzchowski, and C. B. Eom, Appl. Phys. Lett. **93**, 111912 (2008).

[21] Ullrich Pietsch, Václav Hóly, and Tilo Baumbach, *High Resolution X-Ray Scattering:From Thin Films to Lateral Nanostructures* (Springer, Germany, 2004).

[22] Z. Ovadyahu and Y. Imry, Phys. Rev. B **24**, 7439 (1981).

[23] Y. Ando, A. N. Lavrov, S. Komiya, K. Segawa, and X. F. Sun, Phys. Rev. Lett. **87**, 017001 (2001).

[24] M. A. Steiner, G. Boebinger, and A. Kapitulnik, Phys. Rev. Lett. **94**, 107008 (2005).

[25] *Handbook of Ellipsomety*, edited by H. G. Tompkins and E. A. Irene (Springer, Germany, 2005); A. V. Tikhonravov and M. K. Trubetskov, OPTILAYER thin film software, http://www.optilayer.com

[26] M. Abbate, F. M. F. de Groot, J. C. Fuggle, A. Fujimori, O. Strebel, F. Lopez, M. Domke, G. Kaindl, G. A. Sawatzky, M. Takano, Y. Takeda, H. Eisaki, and S. Uchida, Phys. Rev. B **46**, 4511 (1992).

[27] T. Saitoh, A. E. Bocquet, T. Mizokawa, H. Namatame, A. Fujimori, M. Abbate, Y. Takeda, and M. Takano, Phys. Rev. B **51**, 13942 (1995).

[28] G. V. M. Williams, L. Y. Jang, and R. S. Liu, Phys. Rev. B **65**, 064508 (2002).

[29] R. S. Liu, L.-Y. Jang, H.-H. Hung, and J. L. Tallon, Phys. Rev. B **63**, 212507 (2001).

[30] Z. Hu, H. von Lips, M. S. Golden, J. Fink, G. Kaindl, F. M. F. de Groot, S. Ebbinghaus, and A. Reller, Phys. Rev. B **61**, 5262 (2000).

[31] K. Terai, K. Yoshii, Y. Takeda, S. I. Fujimori, Y. Saitoh, K. Ohwada, T. Inami, T. Okane, M. Arita, K. Shimada, H. Namatame, M. Taniguchi, K. Kobayashi, M. Kobayashi, and A. Fujimori, Phys. Rev. B **77**, 115128 (2008).

[32] Y. Choi, D. Haskel, R. E. Camley, D. R. Lee, J. C. Lang, G. Srajer, J. S. Jiang, and S. D. Bader, Phys. Rev. B **70**, 134420 (2004).

[33] J. W. Freeland, J. J. Kavich, K. E. Gray, L. Ozyuzer, H. Zheng, J. F. Mitchell, M. P. Warusawithana, P. Ryan, X. Zhai, R. H. Kodama, and J. N. Eckstein, J. Phys.: Condens. Matter **19**, 315210 (2007).

[34] J. L. Cohn, C. Chiorescu, and J. J. Neumeier, Phys. Rev. B **72**, 024422 (2005); C. Chiorescu, J. L. Cohn, and J. J. Neumeier, *ibid.* **76**, 020404(R) (2007).

[35] E. Granado, C. D. Ling, J. J. Neumeier, J. W. Lynn, and D. N. Argyriou, Phys. Rev. B **68**, 134440 (2003).

[36] H. Meskine, T. Saha-Dasgupta, and S. Satpathy, Phys. Rev. Lett. **92**, 056401 (2004); H. Meskine and S. Satpathy, J. Phys.: Condens. Matter **17**, 1889 (2005).

[37] R. Kilian and G. Khaliullin, Phys. Rev. B **60**, 13458 (1999).